TROPICAL OCEANIC PRECIPITATION FREQUENCY FROM NIMBUS 5 MICROWAVE DATA

by Stanley Q. Kidder

DEPARTMENT OF ATMOSPHERIC SCIENCE

COLORADO STATE UNIVERSITY

FORT COLLINS, COLORADO

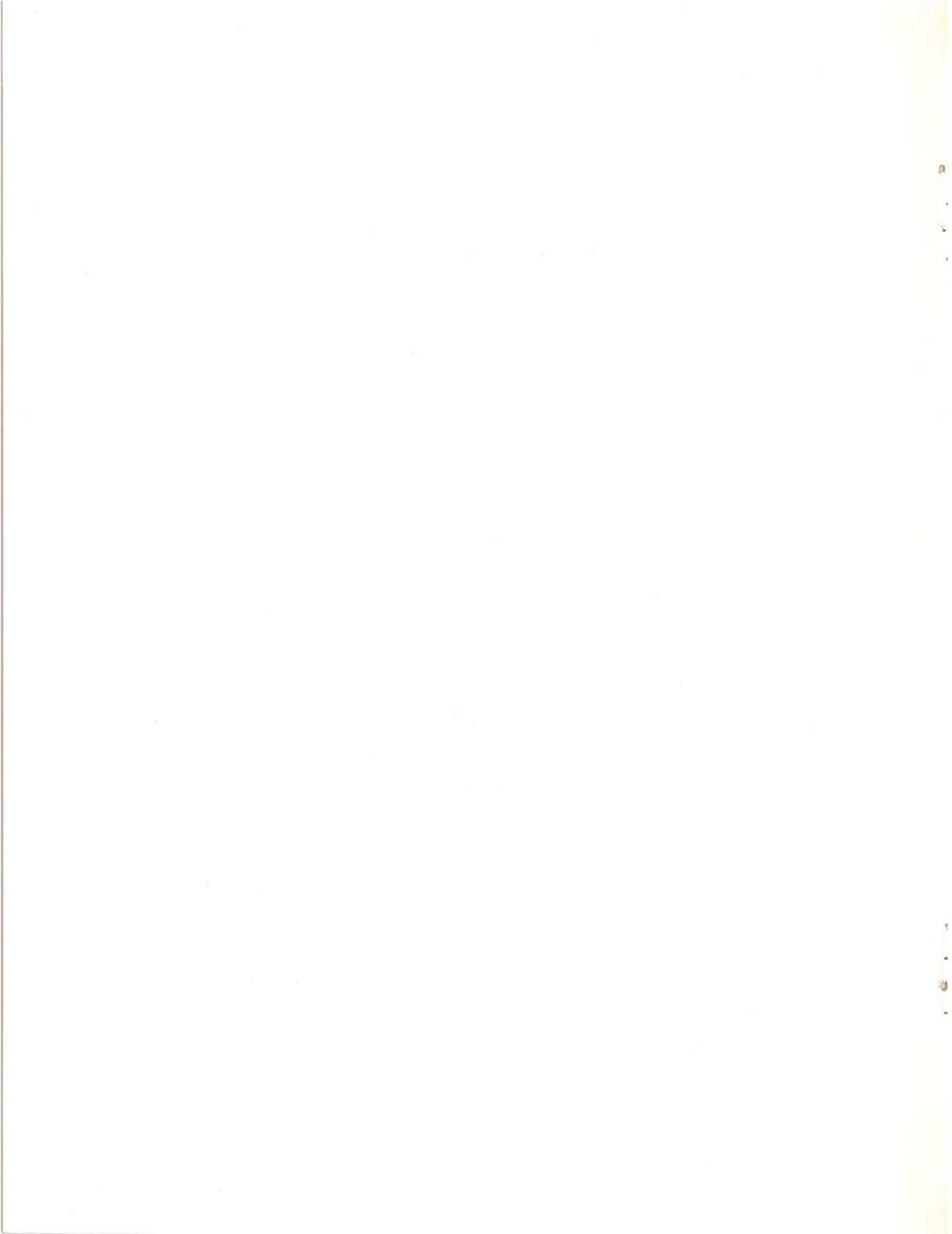TROPICAL OCEANIC PRECIPITATION FREQUENCY
FROM NIMBUS 5 MICROWAVE DATA

by

Stanley Q. Kidder

Department of Atmospheric Science

Colorado State University

Fort Collins, Colorado

May, 1976

Atmospheric Science Paper no. 248

ABSTRACT

Microwave brightness temperature data from the Nimbus 5 satellite have been analyzed, using threshold brightness temperatures, to yield tropical oceanic precipitation frequencies for several classes of rainfall rates during the season December 1972 through February 1973. Data taken near local noon and near local midnight were analyzed. The overall results are consistent with both climatological precipitation frequency and with concurrent satellite-derived frequency of highly reflective clouds. The difference between the local noon and local midnight frequencies is small, but the heavier rainfall rates tend to occur more frequently near local noon. The ratios of the frequencies of light, moderate, and heavy rain were observed to be relatively constant over the tropical oceans. Passive microwave measurements from space seem to be an important step toward accurate measurement of oceanic precipitation.

ACKNOWLEDGEMENTS

TABLE OF CONTENTS

LIST OF FIGURES

LIST OF TABLES

1.0 INTRODUCTION

Knowledge of oceanic precipitation is of fundamental importance to meteorology. Approximately 80% of the earth's precipitation falls in the ocean (Sellers, 1965) where fewer than ten percent of the world's weather stations exist. Yet the latent heat released over the ocean plays a major role in the maintenance of the general circulation and effects almost everything known as "weather".

Many ingenious attempts have been made to determine oceanic precipitation amounts, but all are indirect methods which are only remotely connected with areal precipitation. Many of these efforts rely on extrapolations of island and coastal data (c. f. Jacobs, 1968) which constitute an extremely small sample over the approximately 3.5×10^8 km^2 of ocean. Ships' logs have been used to compile climatological means of such meteorological parameters as wind, cloudiness, precipitation frequency (McDonald, 1938), and even precipitation amounts from qualitative weather (WW) codes (Tucker, 1961). Shipping lanes are such, however, that many data are taken at certain times and places while few are taken elsewhere. More recently satellite data, which is free of many kinds of sampling bias, have been used to estimate precipitation. Until the launch of Cosmos 243 in 1968 and Nimbus 5 in 1972, however, all of the data were from the visible or infrared portions of the electromagnetic spectrum in which precipitation cannot be observed directly due to the opacity of clouds.*

---

*See Martin and Scherer (1973) and Dittberner and Vonder Haar (1973) for a review of precipitation estimation techniques using visible and infrared satellite data.

A solution to the problem of the determination of oceanic precipitation seems to be passive microwave sensing from satellites. Raindrops, being strong emitters and scatterers of microwave radiation, can be detected at satellite altitudes over the ocean even through clouds, which are practically transparent in the microwave region. In this paper, data from the Electrically Scanning Microwave Radiometer (ESMR) aboard Nimbus 5 are used to determine precipitation frequency over the ocean during one season. This is a first step toward measuring latent heat release over oceans, and the results may be directly used to test the operation of numerical models of the general circulation (c. f. Holloway and Manabe, 1971).

2.0 THE TRANSFER OF MICROWAVE RADIATION

2.1 Radiative Transfer Theory

The equation of radiative transfer may be written (Chandrasekhar, 1960):

$$\frac{dN_\lambda(\vec{r},\vec{s})}{dz} = -(\alpha_s + \alpha_a)N_\lambda(\vec{r},\vec{s}) + \alpha_a B_\lambda(T) + \alpha_s \int_0^{4\pi} P(\vec{r},\vec{s},\vec{s}')N_\lambda(\vec{r},\vec{s}')d\Omega_s, \qquad (1)$$

where $N_\lambda(\vec{r},\vec{s})$ is the spectral radiance (power per unit wavelength per steradian per unit area perpendicular to $\vec{s}$) at the point $\vec{r}$ in the direction $\vec{s}$, $B_\lambda(T)$ is the Planck function, α_s and α_a are the volume scattering and absorption coefficients, respectively, $P(\vec{r},\vec{s},\vec{s}')$ is the scattering phase function, and z is the distance along the ray path. Qualitatively, equation (1) gives the rate of change of the radiance along the path at point $\vec{r}$ in terms of 1) the radiance absorbed and scattered out of the beam by the medium, 2) the radiance added to the beam by thermal emission of the medium, and 3) radiance scattered into the beam from other directions. In the microwave region ($\lambda > 1$ mm), N_λ is proportional to equivalent blackbody (or brightness) temperature, T_B, and the Planck function is proportional to local temperature by the Rayleigh-Jeans Law. Therefore, equation (1) becomes

$$\frac{dT_B(\vec{r},\vec{s})}{dz} = -(\alpha_s + \alpha_a)T_B(\vec{r},\vec{s}) + \alpha_a T(\vec{r}) + \alpha_s S_c \qquad (2)$$

where

$$S_c \equiv \int_0^{4\pi} P(\vec{r},\vec{s},\vec{s}')T_B(\vec{r},\vec{s}')d\Omega_s, \qquad (3)$$

The brightness temperature measured by a satellite-borne radio-meter can be obtained by integrating the first order, linear differential equation (2) from the surface to the top of the atmosphere H

$$T_B(\theta) = T_{BO}(\theta)t_{0,H}(\theta) + \int_0^H t_{Z,H}(\theta) \left[\alpha_a T + \alpha_s S_c\right] dZ \tag{4}$$

The factor t is the fractional transmittance through a certain layer,

$$t_{a,b} \equiv e^{-\tau_{a,b}} \tag{5}$$

where the optical depth $\tau_{a,b}$ is given by

$$\tau_{a,b} \equiv \int_a^b (\alpha_s + \alpha_a)\ dZ \tag{6}$$

The argument θ indicates that the path of integration makes an angle θ with nadir, and the subscript o indicates a surface value. The apparent surface brightness temperature, $T_{BO}(\theta)$ consists of two terms: The radiation emitted by and reflected by the surface.

$$T_{BO} = \epsilon(\theta)T_o + T_{BR} \tag{7}$$

where ϵ is the surface emittance, T_o is the surface temperature, and T_{BR} is the reflected sky brightness temperature. The brightness temperature measured by a satellite, then, can be written

$$T_B(\theta) = \left[\epsilon(\theta)T_o + T_{BR}\right] t_{0,H}(\theta) + \int_0^H t_{Z,H}(\theta)(\alpha_a T + \alpha_s S_c)dZ \tag{8}$$

Qualitatively, equation (8) gives the brightness temperature measured by the satellite as the sum of 1) that portion of the apparent surface brightness temperature which is transmitted through the atmosphere and

2) the brightness temperature which is emitted and scattered into the beam along the atmospheric path and then transmitted to the satellite.

2.2 Transfer Through the Cloudy Atmosphere

The three atmospheric constituents which significantly effect the transfer of microwave radiation are 1) oxygen (O_2), 2) water vapor, and 3) liquid water (Westwater, 1972). Figure 1 shows the approximate atmospheric attenuation due to oxygen and water vapor near the earth's surface and at 4 km.* The peaks near 22, 183, and 323 GHz are water vapor rotation lines (Van Vleck, 1947), while the band near 60 GHz and the line at 118 GHz have been described as oxygen (O_2) "spin reorientation" transitions (Herzberg, 1950). Calculations by Westwater (1972) indicate that the clear atmosphere is more than 60% transparent for frequencies less than 50 GHz (Figure 2). At the Nimbus 5 ESMR frequency of 19.35 GHz (1.55 cm) the clear atmosphere is more than 90% transparent even in the moist tropics.

Deirmendjian (1963) has shown that atmospheric liquid water can be divided into two classes: cloud-size drops and precipitation-size drops. In clouds with modal drop radius less than 50 μm (which includes the vast majority of clouds (Fletcher, 1963)) the scattering of microwave radiation with frequencies less than 60 GHz may be neglected in comparison with absorption. Clouds, therefore, may be treated with a simple absorption coefficient, which is proportional to liquid water content (Westwater, 1972). Figure 3 shows the cloud volume absorption coefficient for a $0^{\circ}C$ cloud normalized to $1 g\ m^{-3}$. A lower bound on

---

* Attenuation (A) in db km^{-1} is related to volume absorption coefficient (α_a) in km^{-1} by $\alpha_a = (.1\ \log_e 10)\ A \approx 0.2303A$.
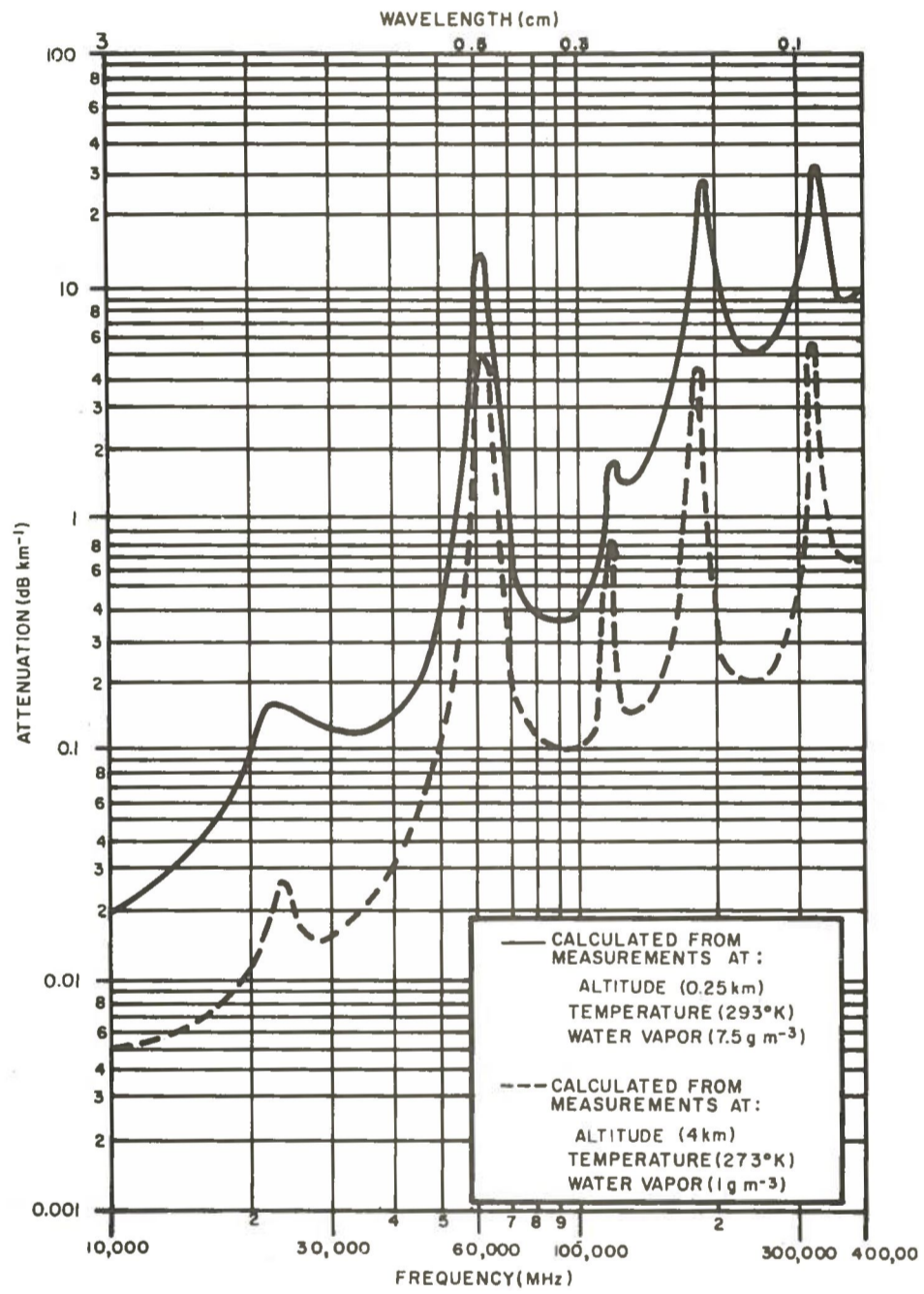
Figure 1. Atmospheric attenuation by combined water vapor
and oxygen (O_2). (After Tolbert et al., 1958)
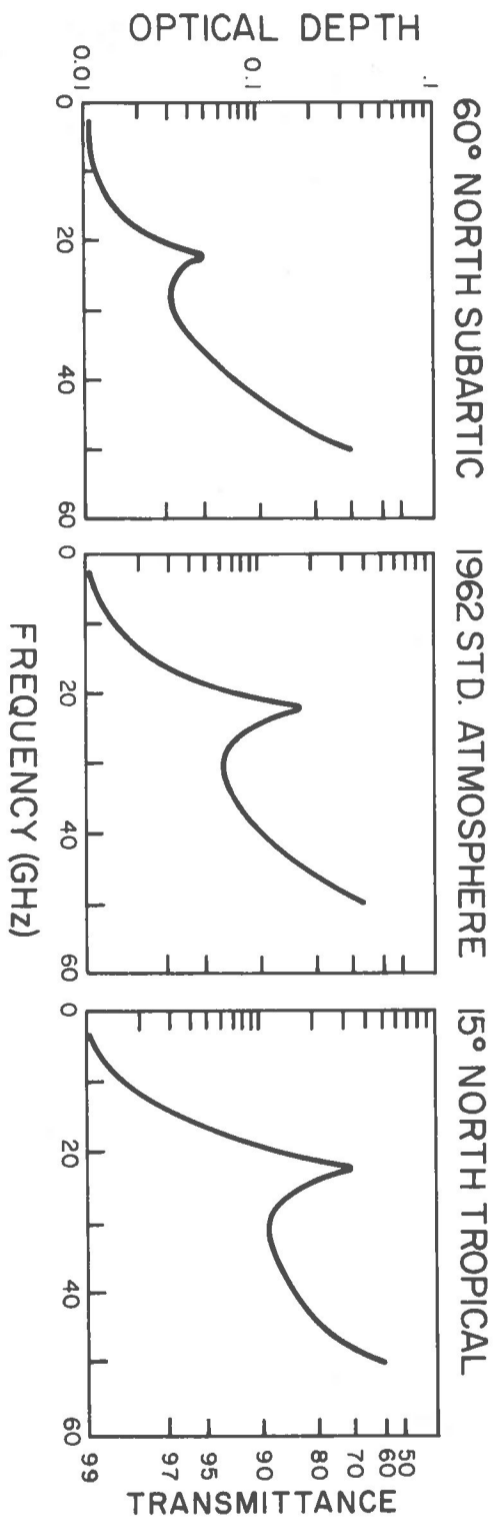
Figure 2. Optical depth of clear atmospheres. (After Westwater, 1972)
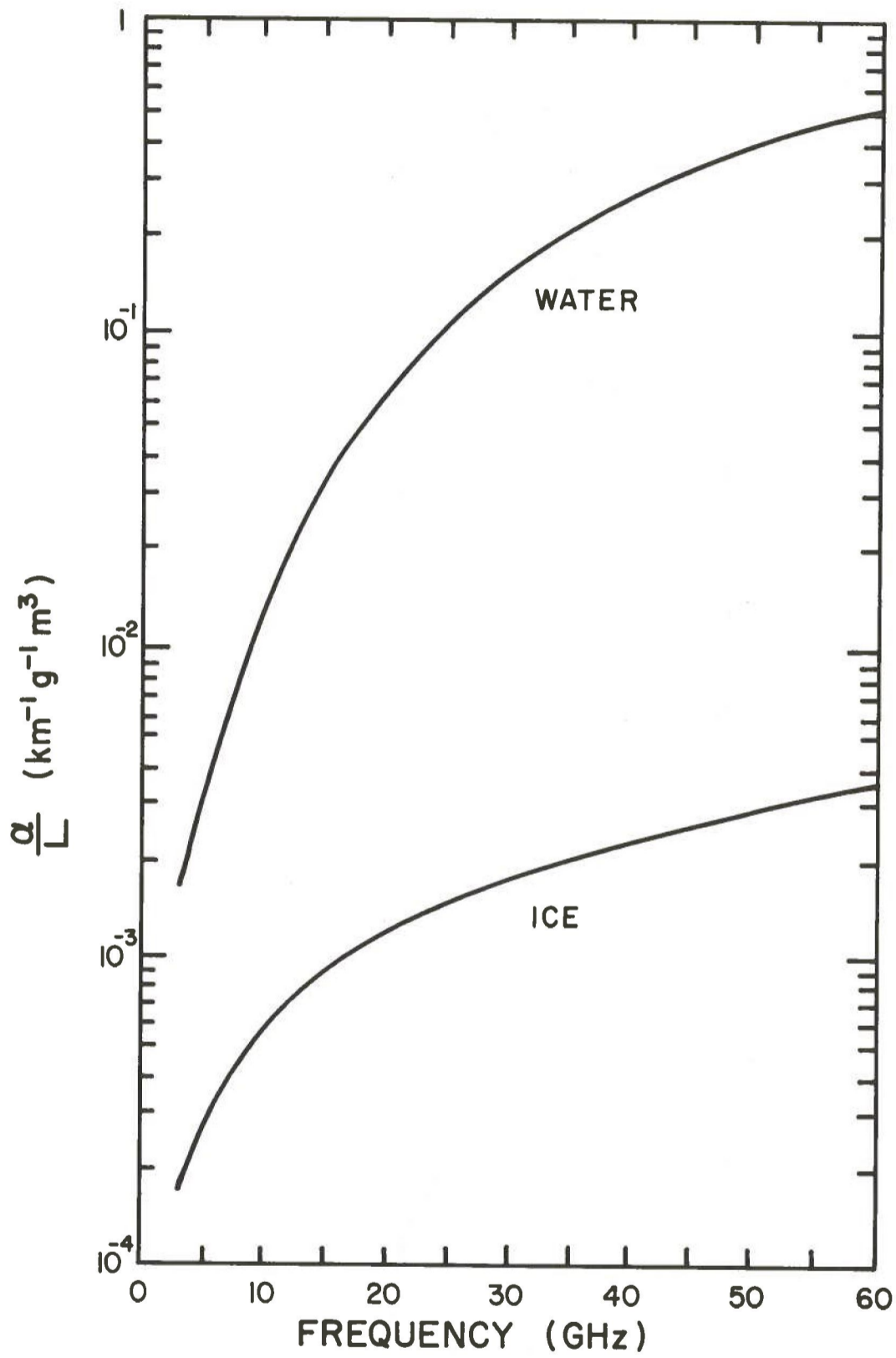
Figure 3. Cloud Optical Depth. (After Westwater, 1972)

cloud transmittance (for nadir viewing) can be obtained as follows

$$\tau_c = \int_0^H \alpha_c \, dZ = \int_0^H \frac{\alpha_c}{L} L \, dZ \tag{9}$$

where L is the density of the cloud droplets. For frequencies less than 50 GHz, the ratio α_c/L is less than 5 $g^{-1}cm^2$, and for 19.35 GHz, α_c/L is less than 0.8 $g^{-1}cm^2$ for a water cloud.* Ignoring the small temperature dependence of α_c/L,

$$\tau_c \approx \frac{\alpha_c}{L} \int_0^H L dZ = \frac{\alpha_c}{L} L_I \tag{10}$$

where L_I is the integrated liquid water content of the cloud. Wilheit (1972) estimates a typical value of L_I for a non-raining cloud to be 0.02 g cm^{-2}. Table 1 summarizes the microwave optical properties of non-raining clouds. The total transmittance of the non-raining atmosphere is the product of the clear atmosphere transmittance and the cloud transmittance. At 50 GHz the transmittance is greater than 46%, and at 19.35 GHz it is greater than 85%. This large transmittance through clouds is the chief advantage of passive microwave radiometry.

2.3 Surface Emission

Because the atmosphere is so transparent to microwave radiation of frequencies less than 50 GHz, the surface term in equation (8) is often dominant; the satellite-measured microwave brightness temperature depends strongly on surface emittance.

---

* Ice clouds are much more transparent than water clouds; c,f. Figure 3.

TABLE 1

Approximate Microwave Transmission
Through Non-Raining Clouds

	Typical Cloud	"Thick" Cloud
Integrated Liquid Water	0.02 g cm^{-2}	0.05 g cm^{-2}
Optical Depth		
50 GHz	0.10	0.25
19.35 GHz	0.02	0.04
Transmittance		
50 GHz	90%	77%
19.35 GHz	98%	96%

The emittance of land is a function of soil type and moisture content, but is generally near 0.9. The emittance of ice and snow is a function of its age, but is also near 0.9 (Wilheit, 1972). Continental and polar regions, therefore, appear bright at frequencies less than 50 GHz. The calm ocean, however, has an emittance of less than 0.5 at these frequencies (Wilheit, 1972 and 1975), which causes it to appear cool in comparison to land or sea ice. The 19.35 GHz calm ocean emittance is approximately 0.4. At wind speeds greater than 7 m s^{-1} foam begins to form on the ocean surface, and the emittance increases. For a 25 m s^{-1} wind Nordberg et al. (1971) found a brightness temperature increase of approximately 22 K (at 19.35 GHz) which corresponds to an emittance increase on the order of 0.1 (25%). The effect of wind-induced brightness temperature increases on precipitation frequency estimates will be discussed in Chapter 4.

Calculations* show that the brightness temperature of a plane water surface varies only slightly with temperature (Figure 4) and thus may be regarded as a constant (approximately 120 K at 19.35 GHz). As a function of incident angle, the emittance of a plane water surface decreases for horizontally polarized radiation (Figure 5) but the decrease is only about 10% for angles out to 35^{0} from nadir. This decrease in emittance is partially compensated by the increase of atmospheric emission caused by the increased path length.

A further consequence of the low ocean emittance is that atmospheric constituents are seen in emission, i.e. increasing the amount of water vapor, oxygen, or the density of water droplets in an atmospheric

---

* See Appendix 1.

BRIGHTNESS TEMPERATURE (KELVIN)

150

140

130

120

110

100

50 GHZ

40 GHZ

30 GHZ

20 GHZ

10 GHZ

0   10   20   30   40

SURFACE TEMPERATURE (CELSIUS)
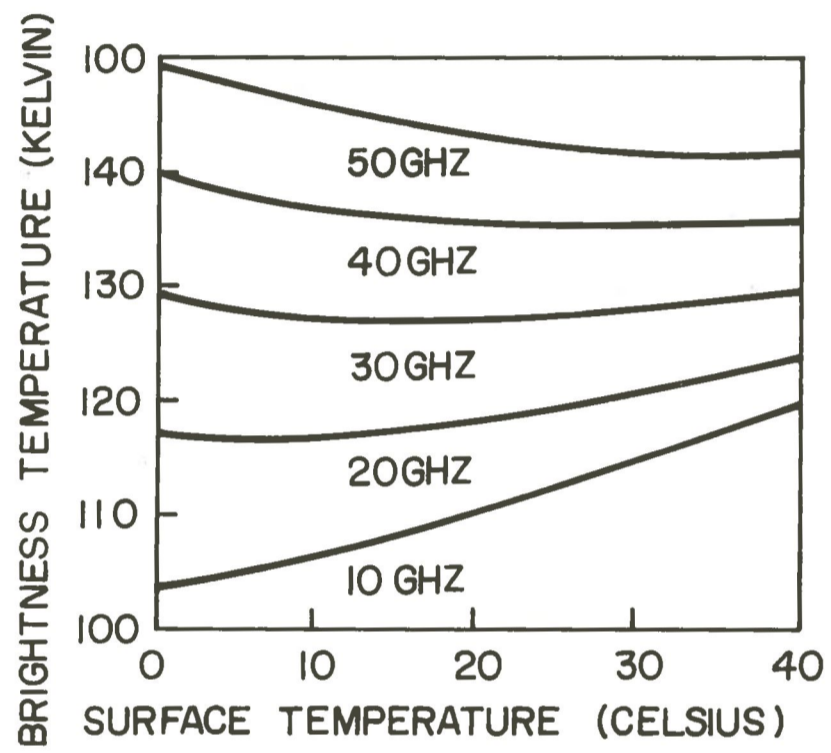
Figure 4. Nadir brightness temperature of
a plane water surface versus
surface temperature.
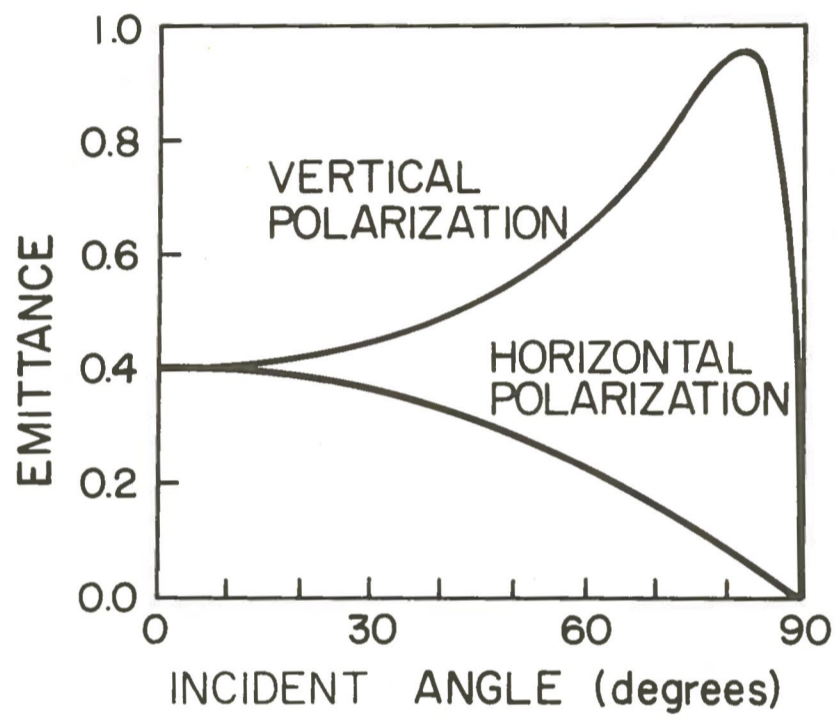
Figure 5.   Emittance of a plane water surface
            versus angle of incidence for a
            wavelength of 1.55 cm and a surface
            temperature of 300 K.

column over the ocean generally increases its brightness temperature.*
The physical explanation of this phenomenon is that the apparent cool-
ness of the ocean in the microwave spectrum causes an overlying atmo-
spheric parcel to be thermodynamically warmer than its radiative
environment; thus it adds to the upwelling radiation stream in the
normal process of absorption and reemission.

The fact that atmospheric constituents are seen in emission at
microwave frequencies over the ocean leads scientists to believe that
passive radiometry might be used to detect these constituents (Shifrin
et al., 1968; Staelin, 1969). Among the possibilities are rainfall
frequency (the subject of this study), rainfall rate, cloud liquid
water, integrated water vapor, and atmospheric temperature.

2.4 Precipitation

Water droplets which are large enough to have significant fall
velocities are large enough to interact strongly with microwave rad-
iation. Scattering, therefore, cannot be neglected in rain layers, and
one must treat the transfer of microwave radiation through these layers
with the full Mie equations (Diermendjian, 1963). Wilheit et al.(1975)
have used a Marshall-Palmer dropsize distribution and Mie scattering
theory to calculate the 19.35 GHz brightness temperature as a function
of rainfall rate and freezing level over the ocean. Their preliminary
results (Figure 6) compare favorable with radar-measured and rain
gauge-measured rainfall rates.

---

* Except at very high rainfall rates. See Figure 6.
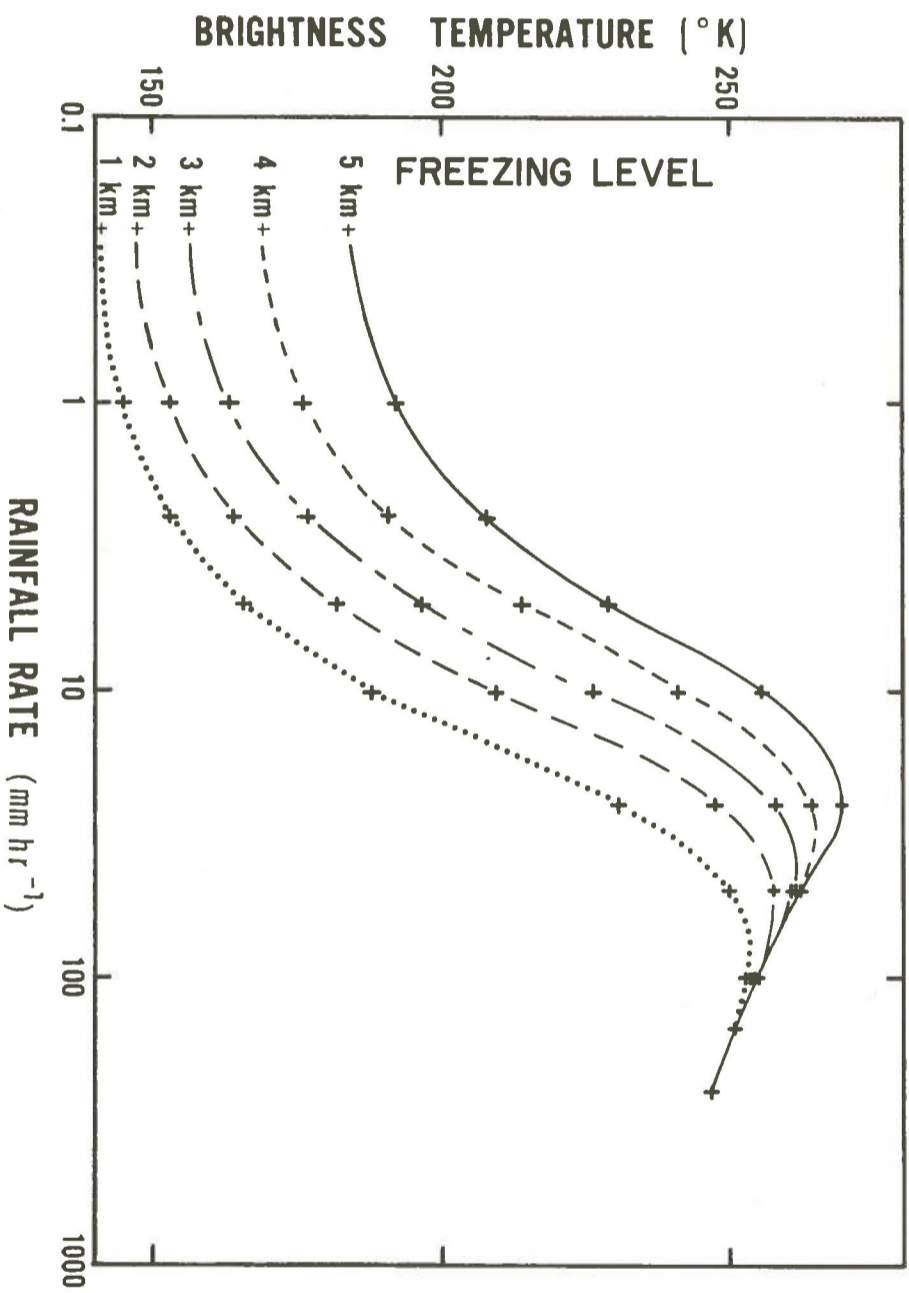
Figure 6. 1.55 cm brightness temperature versus rainfall rate. (After Wilheit et al., 1975)

It should be noted that because the complex part of the index of refraction of ice is much less than that of water, ice clouds are much poorer absorbers of microwave radiation than are water clouds. Thus ice clouds may be neglected when calculating the transfer of microwave radiation (Battan, 1973). Similarly dry snow does not interact well with microwave radiation. While a rain layer is rather opaque at centimeter wavelengths, a dry snow layer is virtually transparent (Battan, 1973). Thus the freezing level may be used to indicate the thickness of the rain layer, and the frozen precipitation above the layer may be ignored in the scattering calculations.

The results of Wilheit et al. form the basis of a thresholding technique used in this paper for the detection of oceanic precipitation described in Section 3.4.

3.0 DATA AND ANALYSIS

3.1 Description of the Radiometer

The Electrically Scanning Microwave Radiometer (ESMR) carried
aboard Nimbus 5 was launched 11 December 1972 into a sun-synchronous
orbit and became operational 19 December 1972. The radiometer consists
of three major components.*

1. A nadir-pointing, phased array antenna (Figure 7) consisting
   of 103 wave guides in a 83.3 cm by 85.5 cm rectangle which
   detects horizontally polarized radiation ($\vec{E}$ parallel to the
   spacecraft velocity vector.)

2. A beam-steering computer which sweeps the received beam from
   50^0 left to 50^0 right of the spacecraft track in 78 steps every
   four seconds by means of an electronic phase shifter in each
   wave guide.

3. A microwave receiver operating with a center frequency of
   19.35 GHz and a bandwidth of 250 MHz. A 10 MHz band centered
   on 19.35 GHz is not received.

The ground resolution is 25 km by 25 km at nadir, approximately
42 km crosstrack by 30 km downtrack at 30^0 from nadir, and degrades to
160 km crosstrack by 45 km downtrack at 50^0 from nadir (Figure 8).
Thus an ESMR scan spot covers approximately 500 km^2 at nadir and 1000
km^2 at 30^0 from nadir.

The Nimbus 5 orbit (81^0 retrograde inclination, approximately
1100 km altitude) is such that ESMR views every point on earth at
least twice per day (if one uses all of the data from $\pm50^0$ from nadir).
It crosses the equator at 1130** (ascending) and 2330*** (decending)

---

   * See Wilheit (1972) for a more complete description.

  ** "Noon"

*** "Midnight"

NIMBUS 5

YAW NOZZLE

SOLAR ARRAY SUN SENSOR

TRACKING & DATA RELAY EXPERIMENT (T&DRE) ANTENNA DUMMY

SUN

PITCH NOZZLE

PNEUMATICS ASSEMBLY

DIRECTION IN ORBIT

HORIZON SCANNER

AUXILIARY LOAD PANEL

RIGHT SOLAR PADDLE

INTERCONNECTING TRUSS

THERMAL CONTROL SHUTTERS

VERSATILE INFORMATION PROCESSOR (VIP) BEACON ANTENNA

NEMS SPACE RADIATORS

NIMBUS E MICROWAVE SPECTROMETER (NEMS)

S-BAND ANTENNAS

TEMPERATURE HUMIDITY INFRARED RADIOMETER (THIR)

INFRARED TEMPERATURE PROFILE RADIOMETER (ITPR)

ELECTRICALLY SCANNING MICROWAVE RADIOMETER (ESMR) (DEPLOYED POSITION)

LEFT SOLAR PADDLE

SELECTIVE CHOPPER RADIOMETER (SCR)

SURFACE COMPOSITION MAPPING RADIOMETER (SCMR)

Figure 7.   The Nimbus 5 spacecraft.   (from <u>The Nimbus 5 User's Guide</u>.)
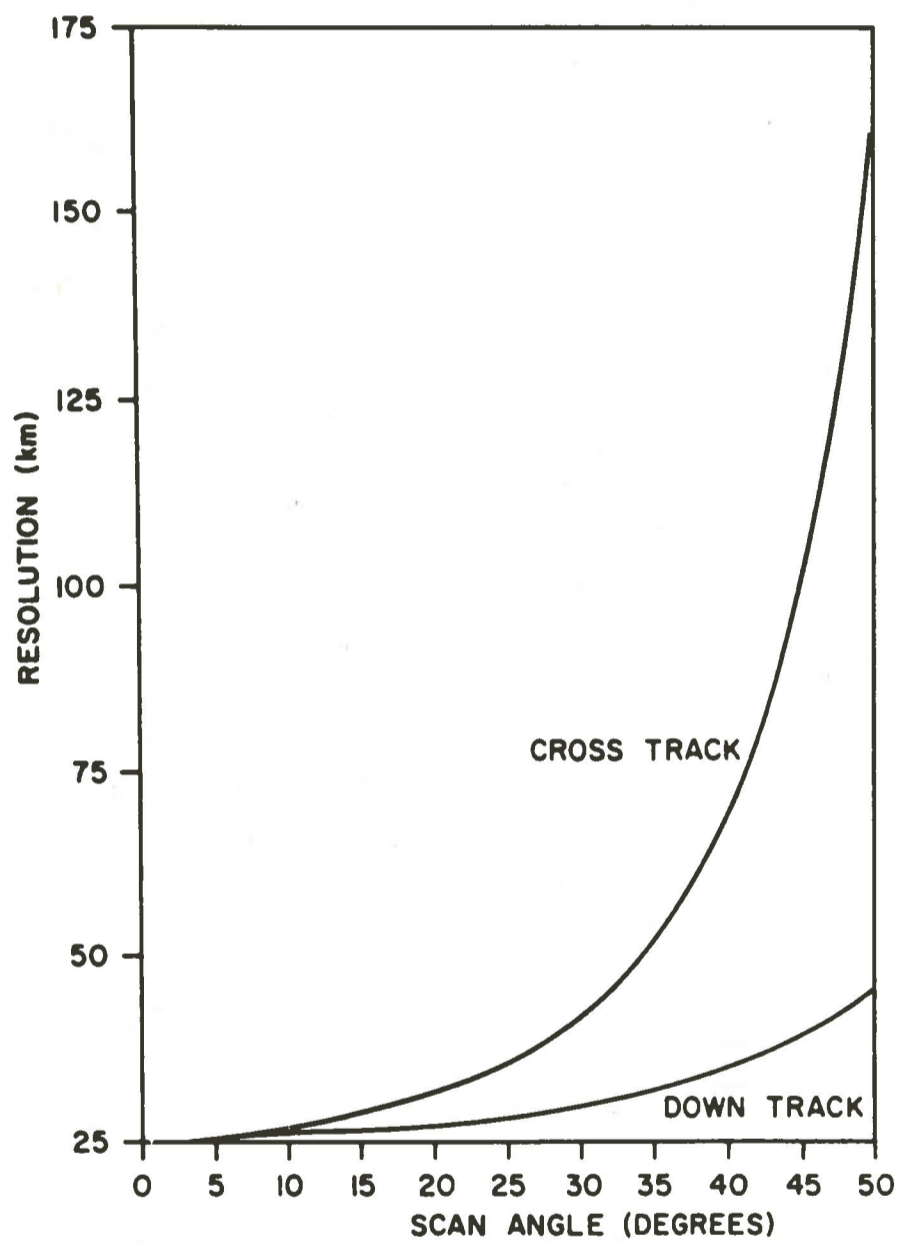
Figure 8. Resolution of the Electrically Scanning
Microwave Radiometer. (After Wilheit, 1972)

local time and has an orbital period of approximately 107 minutes.
Additional ESMR characteristics are noted in Appendix 2.

Figure 9 is a montage of photographically processed ESMR data
from The Nimbus 5 Data Catalog, Vol. 1 in which brightness temperatures
greater than 250 K appear black, those less than 190 K appear white,
and those in between are represented with a linear gray scale. The
darkest regions over the ocean are areas of intense rain, while the
gray areas represent lighter rainfall rates (See Figure 6). Cloudy
but non-raining areas have brighness temperatures less than 190 K and
thus cannot be seen in this picture.

3.2 The Data Set

The Nimbus 5 ESMR data used in this study were recorded during the
period 22 December 1972 through 26 February 1973. Approximately one
half of the available data were randomly selected for study to reduce
the bulk processing. Figure 10 shows the distribution of the selected
data in number of orbits per day -- 13 1/3 being the maximum daily
number. The data are recorded on Calibrated Brightness Temperature
(CBT) Tapes* which contain the position (latitude, longitude) of each
scan spot, time, subsatellite point, and various calibration data in
addition to the brightness temperatures.

---

* These tapes are available from The National Space Science Data
Center, Greenbelt, MD, and are described in detail in The Nimbus 5 User's
Guide and The Nimbus 5 Data Catalog.

Figure 9.   Photographically processed Nimbus 5 ESMR data from 11 January 1973, orbits
            413-425.   Brightness temperatures less than 190 K are white, those greater
            than 250 K are black, and those in between are represented by a linear gray
            scale.   Rain, which appears dark over the ocean is evident in the tropics
            and in several weather fronts. (From The Nimbus 5 Data Catalog, Vol. 1)
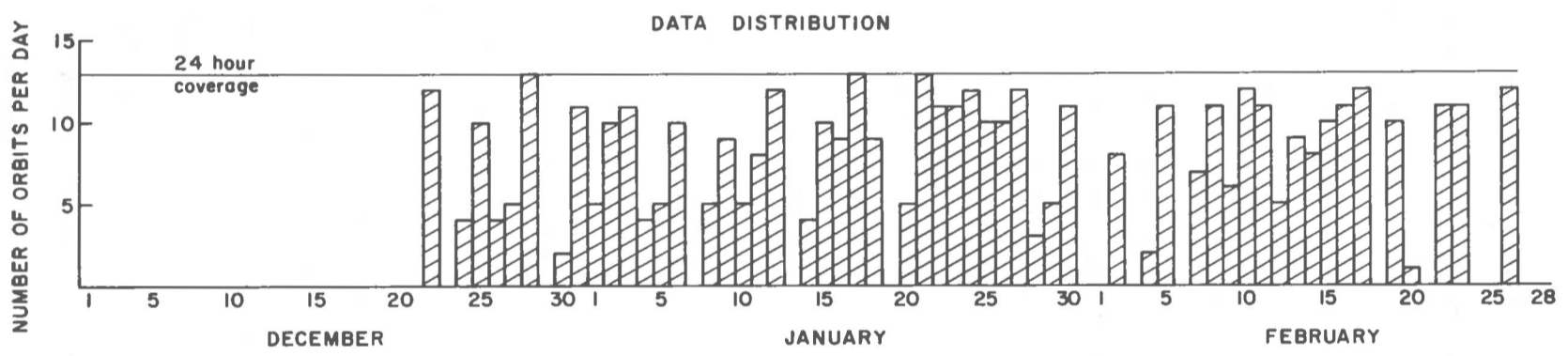
Figure 10.   Distribution of the Nimbus 5 ESMR data used in this study

3.3 Angular Corrections

To eliminate a cross-polarization lobe problem with the ESMR antenna, the brightness temperatures on the CBT Tapes have been corrected by the National Aeronautics and Space Administration (NASA) with a linear empirical correction first described in Volume 2 of The Nimbus 5 Data Catalog. NASA's correction was applied to all of the data regardless of surface type or local time while the CBT Tapes were being made. No correction was found necessary near nadir.

In the course of this study it was determined that the correction applied by NASA does not fully eliminate the problem of brightness temperature variation with scan angle over the ocean. We also found that there is a small offset between midnight and noon data. To examine and hopefully resolve these problems, the Pacific Ocean data were partitioned into 10^0 latitude-longitude squares and the mean brightness temperature for the three months was calculated as a function of the scan angle for each square. Then the difference between the mean brightness temperature at scan angle θ and the mean brightness temperature at nadir (actually the two beam positions at $\pm$ 0.6^0 from nadir) was averaged over all 104 10^0 latitude-longitude squares and plotted versus θ. The results for the local noon data are shown in Figure 11a. When the local midnight data were analyzed, they were found to be cooler than the local noon data. In 15 squares which receive little rain, the average difference between the noon and midnight brightness temperatures was found to be 5.8 K $\pm$ 0.9 K. Figure 11b shows the mean midnight T_B versus θ data, but the curve has been shifted down 5.8 K to correct for the apparent day-night temperature difference which is not physically reasonable. The two curves in Figure 11 constitute
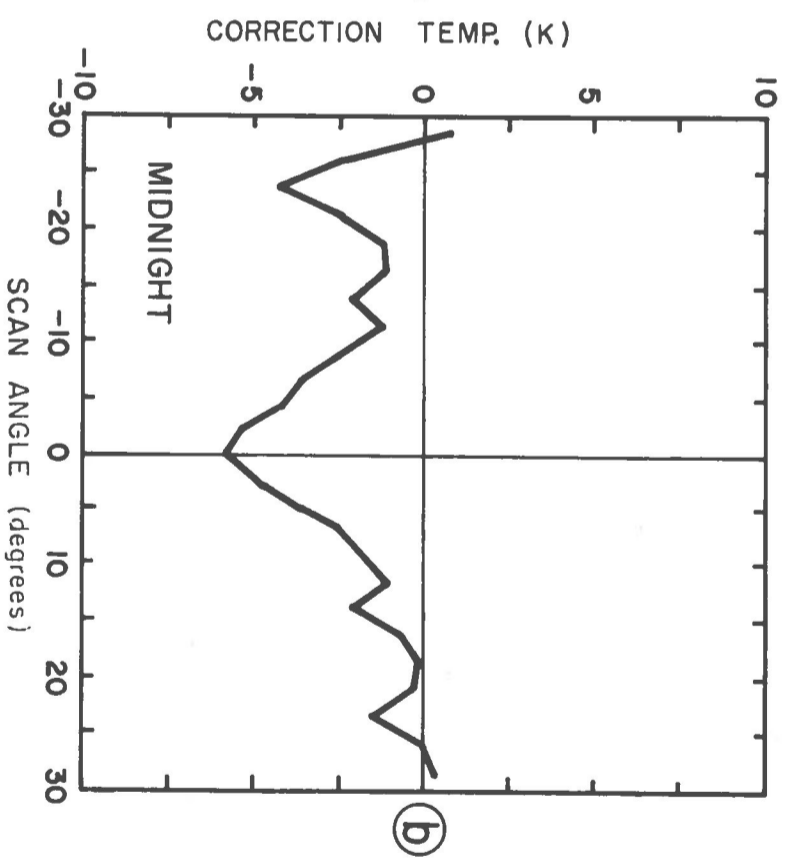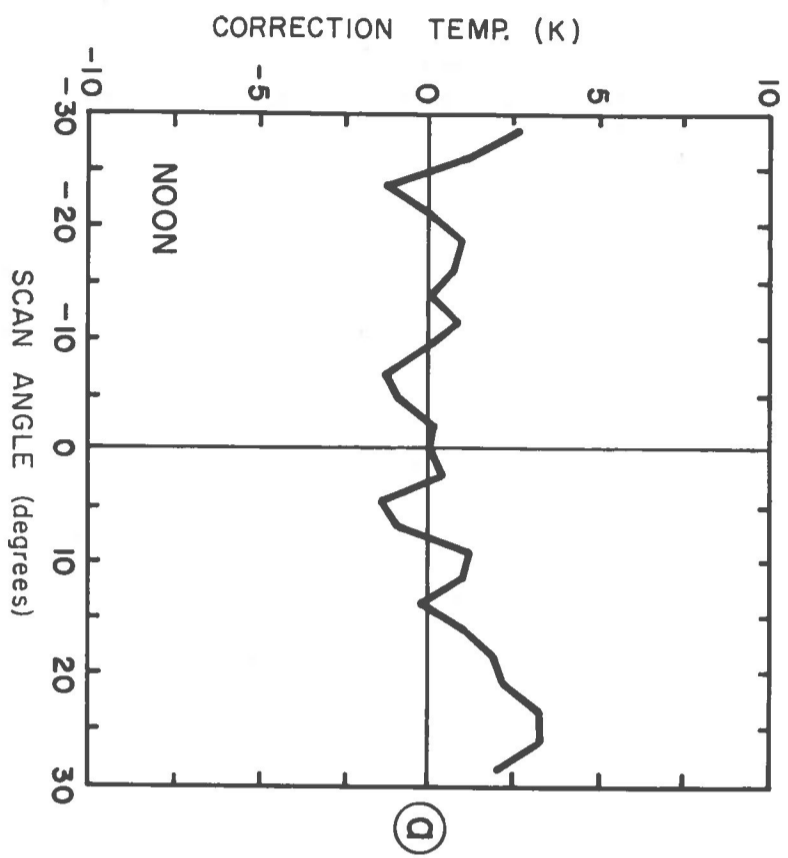
Figure 11. Scan angle correction temperatures, (a) noon correction, (b) midnight correction.

correction curves which will make the three-month mean brightness temperatures independent of scan angle and local time. Table 2 lists the exact correction temperatures used.* These temperatures were sub-tracted from the temperatures in the CBT Tapes before application of the thresholding technique described below.

3.4 The Use of a Threshold Brightness Temperature to Detect Oceanic Precipitation

Radiative transfer theory predicts that at 1.55 cm a rain layer should appear bright against the cold background of the ocean. The photographically processed Nimbus 5 ESMR data corroborates this theory. The purpose of this study was to determine a threshold brightness temp-erature which can be used to detect oceanic precipitation and to use this temperature to calculate seasonal mean precipitation frequencies for the oceans.

Because the seasonal mean freezing level is zonal in character (Figure 12), zonal mean freezing levels (Figure 13, Table 3) were combined with the brightness temperature-rainfall rate curves of Wilheit et al. (1975) (Figure 6) to yield zonal threshold temperatures for the detection of five rainfall rates (Figure 14, Table 4).

The algorithm for calculating precipitation frequencies is the following. For each oceanic 5° latitude-longitude square between 30°N and 30°S the brightness temperature data from the CBT Tapes are first corrected for scan angle with the correction listed in Table 2 and then

---

* In the above-mentioned analysis program, data for two adjacent beam positions were combined. Thus the correction is actually an aver-age for the two beam positions and the same correction is applied to each beam position.

TABLE 2

Scan Angle Correction Temperatures
(To be subtracted from CBT Tape data)

Beam Positions	Nominal Scan Angles	Temperature Correction (K)	
		Noon	Midnight
	(degrees)		
15-16	-29.2 & -27.9	2.7	0.8
17-18	-26.6 & -25.3	1.0	-2.5
19-20	-24.1 & -22.8	-1.2	-4.4
21-22	-21.6 & -20.4	0.1	-2.5
23-24	-19.2 & -18.0	1.0	-1.2
25-26	-16.8 & -15.6	0.8	-1.1
27-28	-14.4 & -13.2	0.0	-2.1
29-30	-12.1 & -10.9	0.8	-1.2
31-32	-9.7 & -8.6	-0.1	-2.4
33-34	-7.4 & -6.3	-1.3	-3.5
35-36	-5.1 & -4.0	-0.9	-4.1
37-38	-2.9 & -1.7	0.1	-5.3
39-40	-0.6 & 0.6	0.0	-5.8
41-42	1.7 & 2.9	0.4	-4.9
43-44	4.0 & 5.1	-1.4	-3.8
45-46	6.3 & 7.4	-0.9	-2.4
47-48	8.6 & 9.7	1.2	-1.7
49-50	10.9 & 12.1	1.0	-1.0
51-52	13.2 & 14.4	-0.3	-2.1
53-54	15.6 & 16.8	1.0	-0.6
55-56	18.0 & 19.2	1.9	-0.1
57-58	20.4 & 21.6	2.2	-0.2
59-60	22.8 & 24.1	3.2	-1.4
61-62	25.3 & 26.6	3.3	0.1
63-64	27.9 & 29.2	1.9	0.4
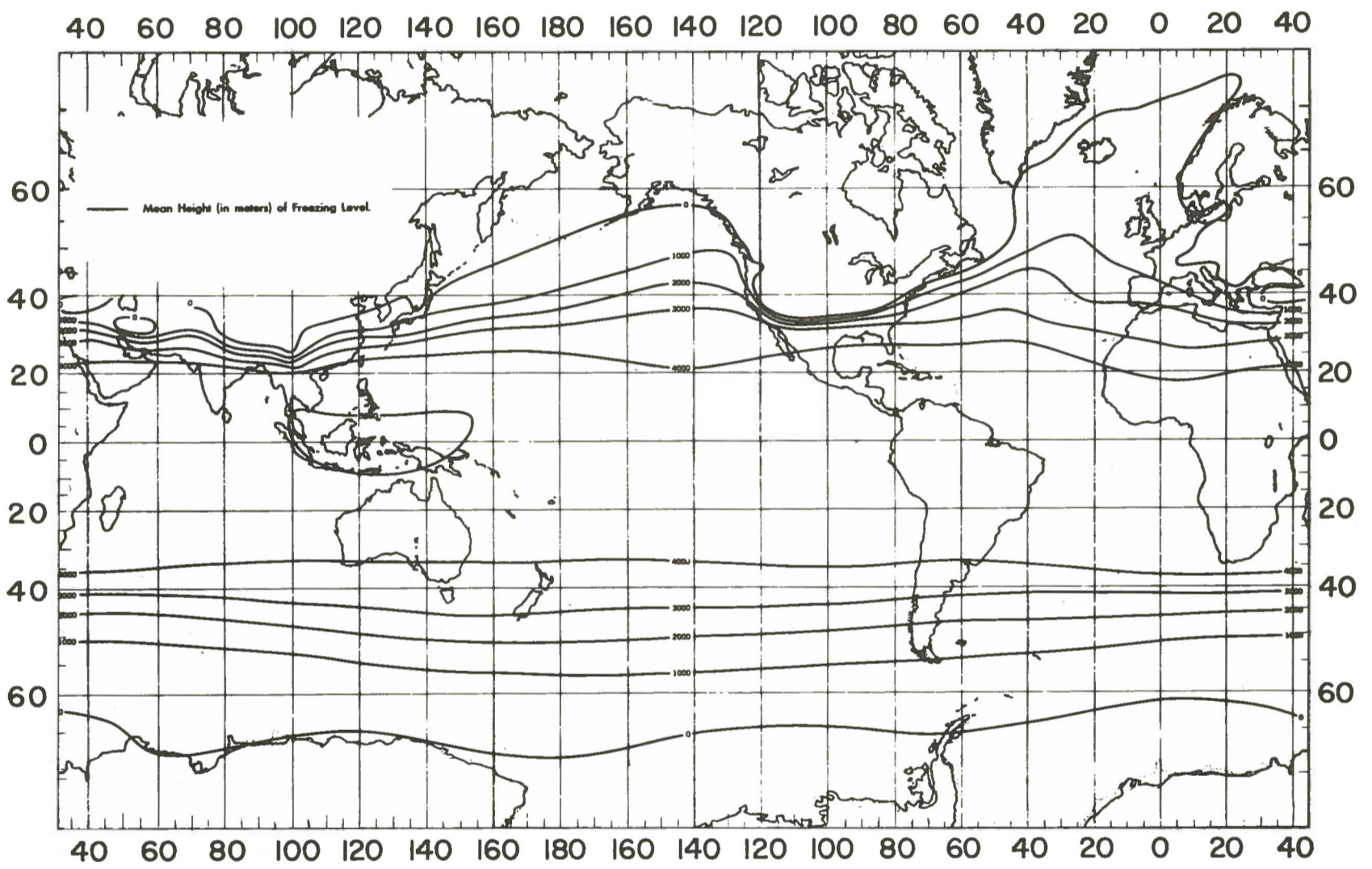
Figure 12. Mean freezing level for the season December-January-February. (After Crutcher and Davis, 1969)
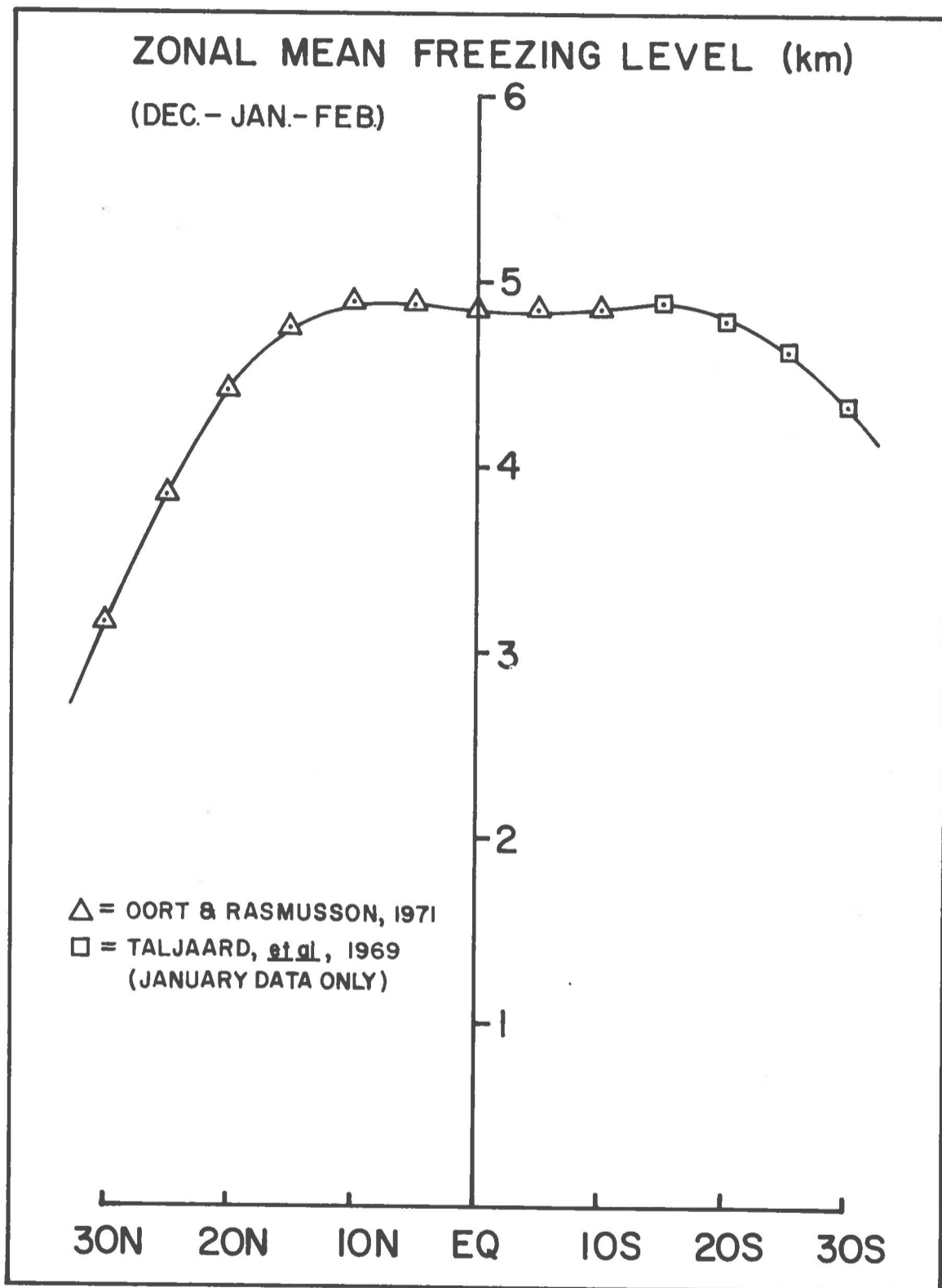
Figure 13. Zonal mean freezing levels for the season December-January-February. (After Oort and Rasmussen, 1971 and Taljaard et al., 1969)

TABLE 3

Zonal Mean Freezing Levels for the Season
December-January-February. (After Oort
and Rassmussen, 1971; and Taljaard et al., 1969)

Zone	Mean Freezing Level (km)
$30^{o}S - 25^{o}S$	4.48
$25^{o}S - 20^{o}S$	4.71
$20^{o}S - 15^{o}S$	4.84
$15^{o}S - 10^{o}S$	4.89
$10^{o}S - 5^{o}S$	4.87
$5^{o}S - EQ$	4.86
$EQ - 5^{o}N$	4.86
$5^{o}N - 10^{o}N$	4.88
$10^{o}N - 15^{o}N$	4.81
$15^{o}N - 20^{o}N$	4.58
$20^{o}N - 25^{o}N$	4.13
$25^{o}N - 30^{o}N$	3.50

Figure 14. Zonal 1.55 cm threshold brightness temperatures for the detection of oceanic precipitation during the season December-January-February.

TABLE 4

1.55 cm Zonal Threshold Brightness Temperatures
For the Detection of Oceanic Precipitation
During the Season December-January-February

| Zone | Threshold Brightness Temperature (K) | | | | |
	0.25 mm hr^{-1}	0.5 mm hr^{-1}	1.0 mm hr^{-1}	2.5 mm hr^{-1}	5.0 mm hr^{-1}
30°S - 25°S	176.6	178.8	183.6	198.4	222.1
25°S - 20°S	180.0	182.5	187.3	202.3	225.5
20°S - 15°S	181.9	184.5	189.4	204.7	227.1
15°S - 10°S	182.6	185.4	190.3	205.7	227.7
10°S - 5°S	182.4	185.0	189.9	205.3	227.5
5°S - EQ	182.2	184.9	189.8	205.1	227.4
EQ - 5°N	182.2	184.9	189.8	205.1	227.4
5°N - 10°N	182.5	185.2	190.1	205.5	227.6
10°N - 15°N	181.5	184.1	188.9	204.2	226.8
15°N - 20°N	178.1	180.4	185.2	200.0	223.6
20°N - 25°N	171.4	173.4	178.2	192.9	216.3
25°N - 30°N	162.7	164.6	169.4	184.0	205.2

are compared with the threshold temperatures listed in Table 4. Only
data with scan angles between $\pm$ 30^0 from nadir are used. The number of
observations which lie above each of the threshold temperatures is re-
corded along with the total number of observations, midnight and noon
observations being kept separate. The results are presented and dis-
cussed in the next chapter.

4.0 RESULTS

4.1 Tropical Oceanic Precipitation Frequency

Figure 15 shows the frequency, in percentage of observations, of oceanic precipitation for the season December 1972 through February 1973 based on the assumption that the 0.25 mm hr^{-1} brightness temperatures in Table 4 represent the rain - no rain threshold temperatures. (The noon and midnight frequencies have been averaged.) Several expected characteristics of oceanic precipitation are readily apparent:

1. Narrow convergence zones extending around the earth near the equator.

2. Dry eastern oceans.

3. The splitting of the Intertropical Convergence Zone (ITCZ) in the mid-Pacific and a tendancy for such splitting in the western Atlantic.

4. A mid-Pacific maximum in precipitation frequency (23% in the 5° latitude-longitude square centered at 7.5°S, 172.5°W.)

These results may be compared with the data of McDonald (1938) who compiled 50 years of ship log weather observations taken at Greenwich noon. A portion of his Chart 95 is shown in Figure 16. Although McDonald found generally higher frequencies, the overall agreement is good. His maximum frequency is approximately 30% at 7°S, 163°E. More recently Taylor (1973) has compiled An Atlas of Pacific Islands Rainfall, which gives an indication of oceanic precipitation frequencies, (see below). Figure 17 shows the mean January precipitation in millimeters. The contours are very similar to those of Figure 15; but, again, the Pacific precipitation maximum during the season December 1972 through February 1973 was approximately 20° east of its normal position.

C.S. Ramage (1975) points out, however, that December 1972 through February 1973 was an anomalous period in the tropical Pacific (if not
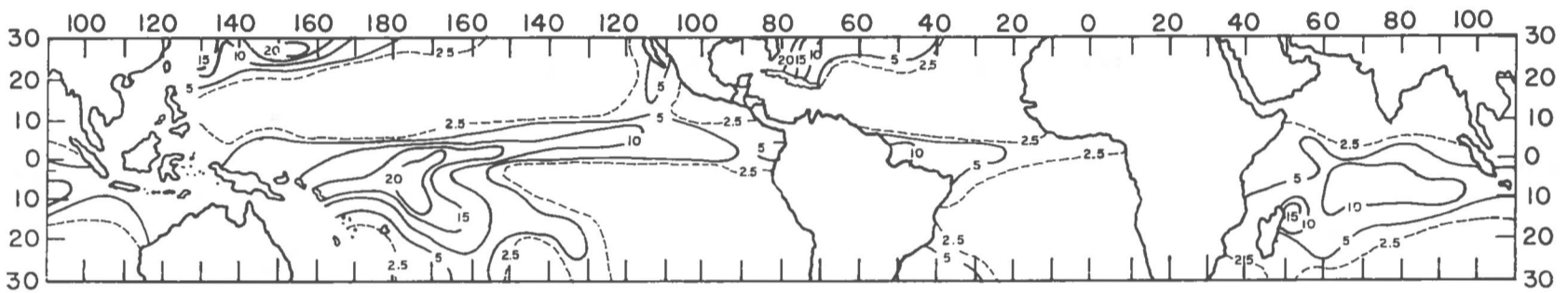
Figure 15.   Frequency of precipitation (in percent of observations) for the season December 1972 through February 1973 as derived from Nimbus 5 ESMR data. (The noon and midnight frequencies have been averaged).
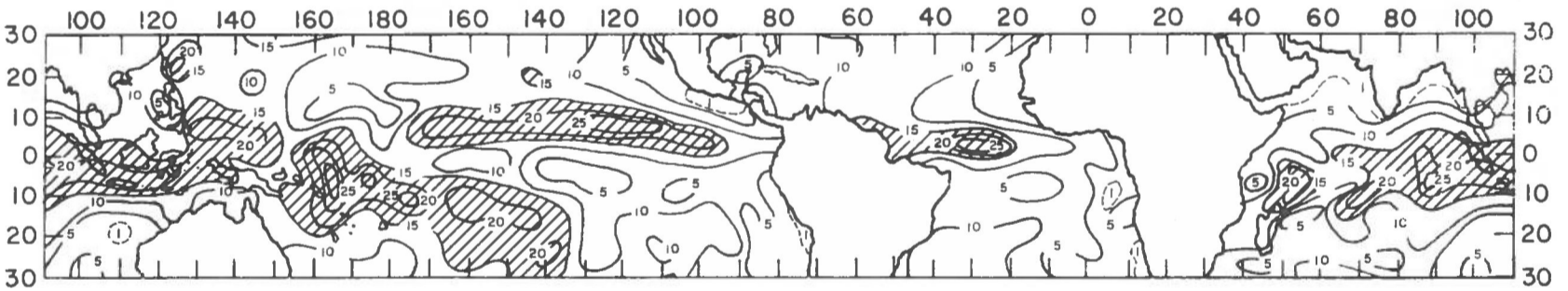

Figure 16.   Frequency of precipitation (in percent of observations) for the season December-January-February from ship observations taken at Greenwich noon. (After McDonald, 1938).
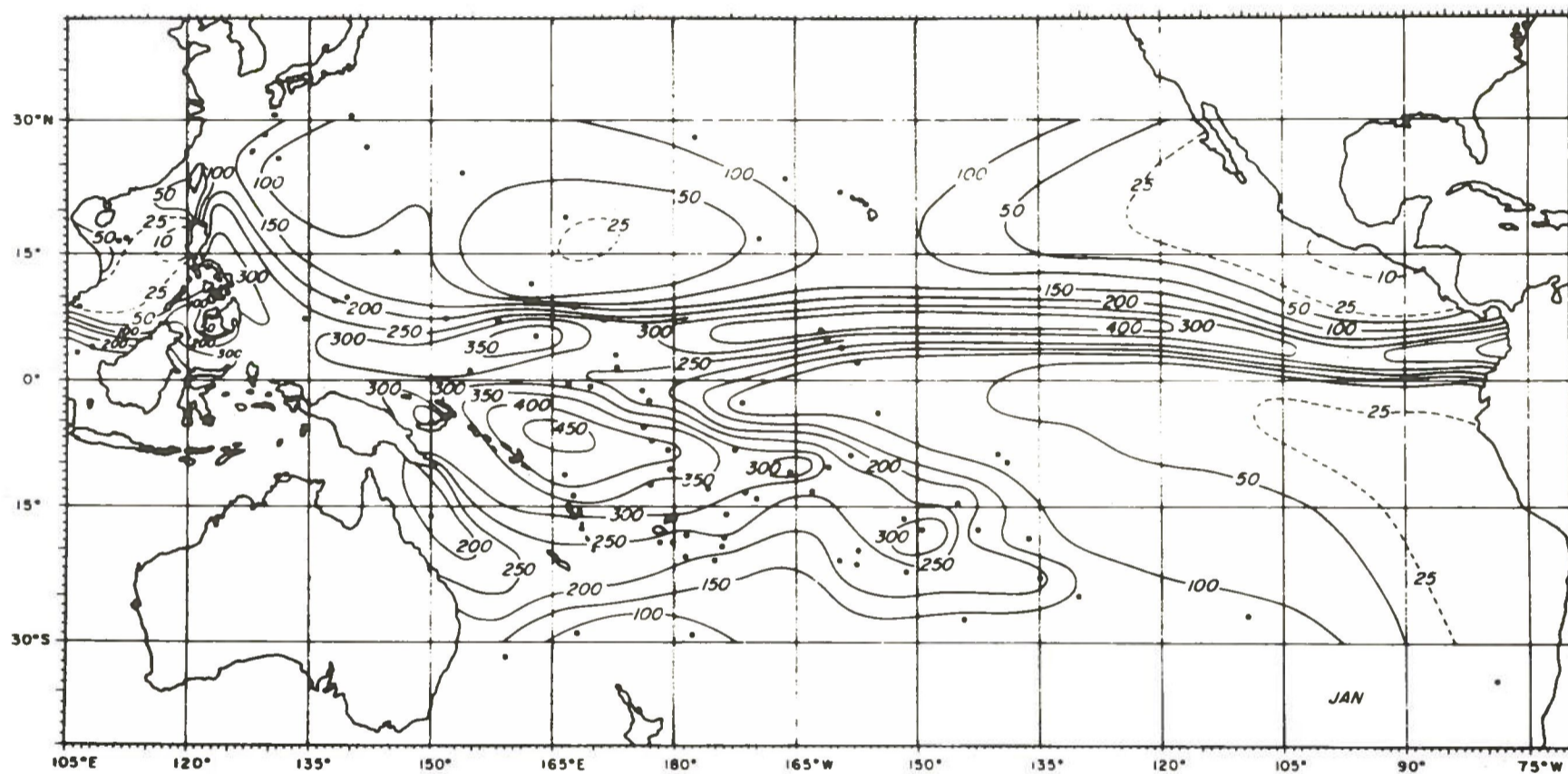
Figure 17. Mean January precipitation (mm). (After Taylor, 1973)

34

in the entire world). In this study of the 1972-1973 El Niño, Ramage
calculated the frequency of highly reflective clouds from National
Environmental Satellite Service daily digitized visible cloud pictures
(Figures 18 and 19). Although the connection between visible cloud
brightness and precipitation is much less clear physically than that
between microwave brightness temperature and precipitation, Figures
18 and 19 show that the cloudiness distribution in December 1972 (the
contours of which closely resemble the contours of precipitation
frequency found in this study) are rather different from the more
normal distribution in December 1971.

As mentioned in Chapter 3, wind, by causing foam formation on the
sea surface, can increase the microwave brightness temperature and
bias precipitation frequency measurements. An estimate of the magni-
tude of this problem can be obtained from Figure 20 which shows the
frequency of Beaufort force 7 (15.5 m s^{-1}) or higher winds at Greenwich
noon in January (after McDonald, 1938). Throughout most of the tropical
oceans there does not seem to be frequent enough wind to significantly
bias the results of this study. However, the northwest oceans seem to
have more frequent winds, thus the precipitation frequencies for those
areas may be overestimated.

Using the other threshold temperatures in Table 4, one can investi-
gate the frequencies of occurrence of various rainfall intensities.
Figures 21 through 23 were constructed by stratifying the data using
0.25 mm hr^{-1} as the threshold for light rain, 1.0 mm hr^{-1} for moderate
rain, and 2.5 mm hr^{-1} for heavy rain. (Again, noon and midnight fre-
quencies were averaged.) This stratification places approximately one
third of the total rain observations in each category. Generally the
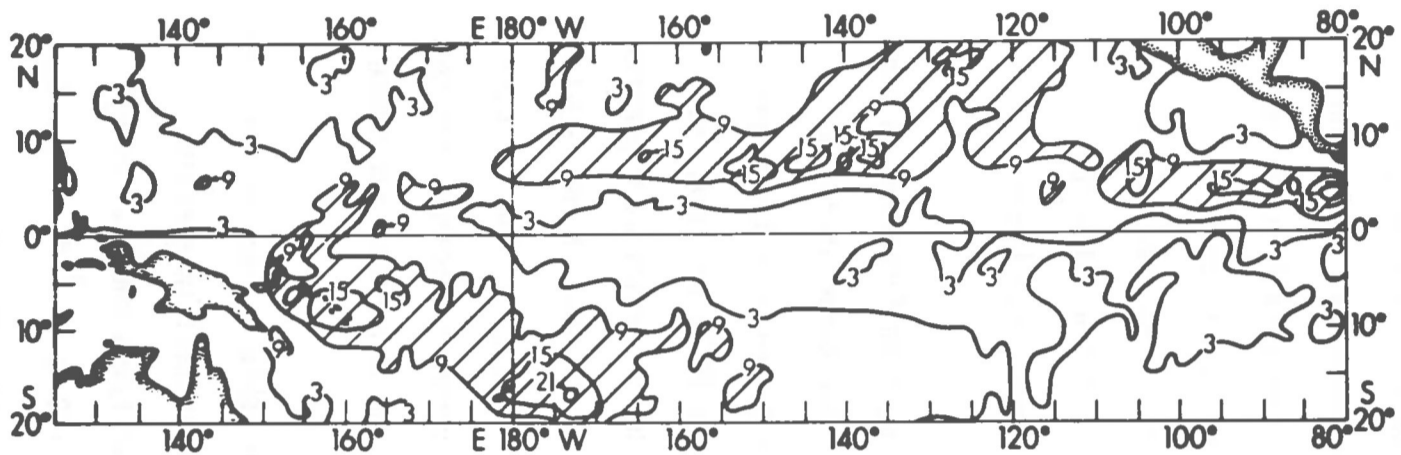
Figure 18. Frequency of highly reflective clouds for December 1971. (After Ramage, 1975)
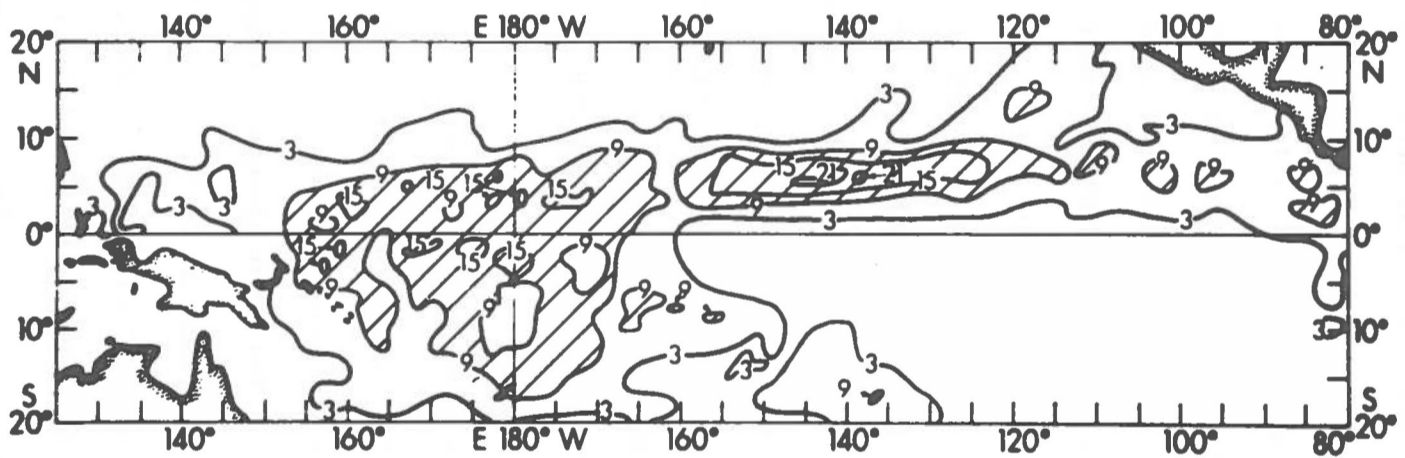
Figure 19. Frequency of highly reflective clouds for December 1972. (After Ramage, 1975)
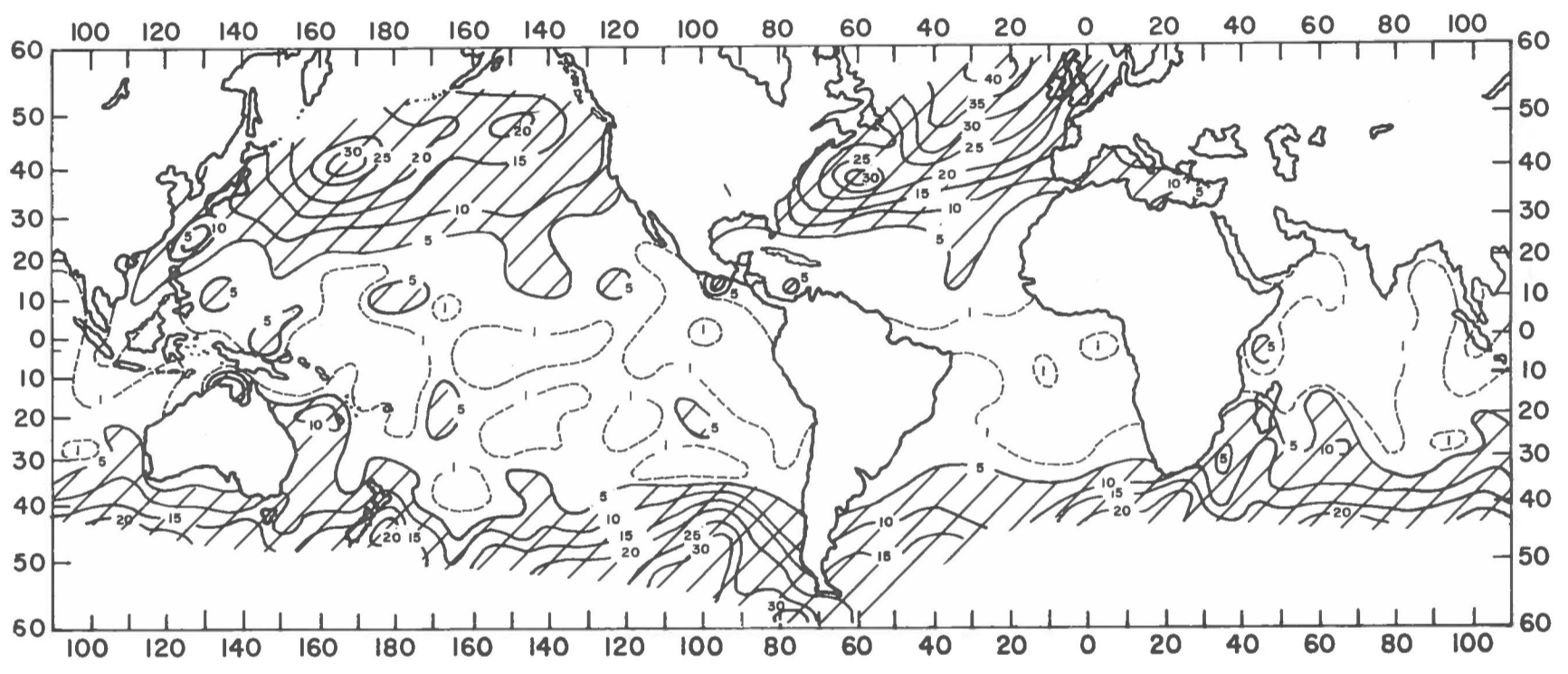
Figure 20. Frequency of Beaufort force 7 (15.5 m s^{-1}) or higher winds at Greenwich noon. (After McDonald, 1938).
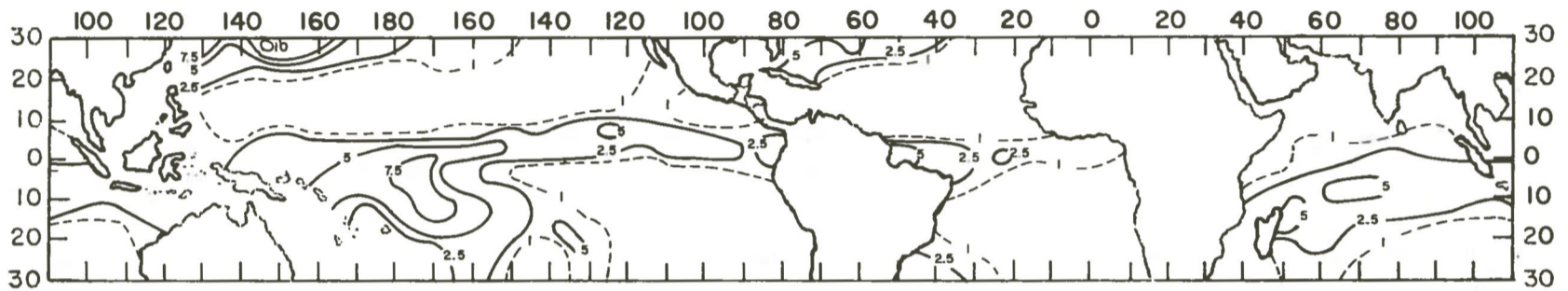
Figure 21. Frequency of light precipitation for the season December 1972 through February 1973. (The noon and midnight frequencies have been averaged).
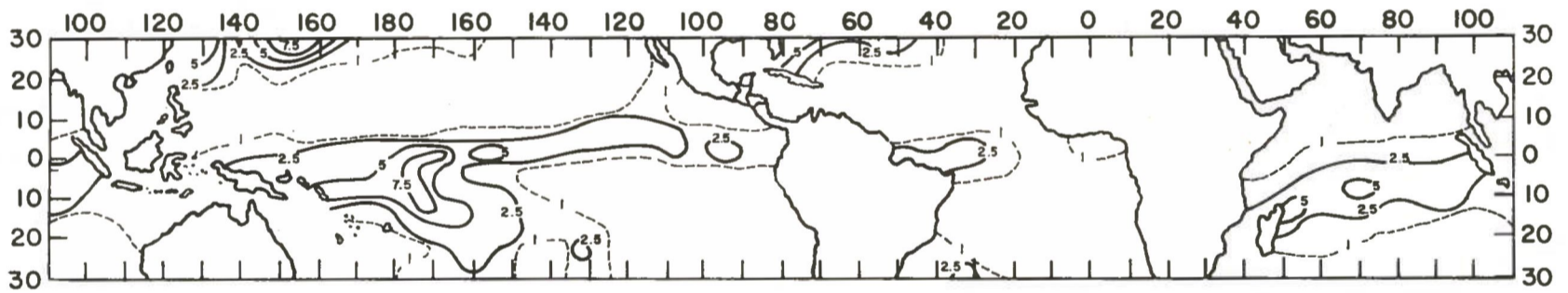
Figure 22. Frequency of moderate precipitation for the season December 1972 through February 1973. (The noon and midnight frequencies have been averaged).
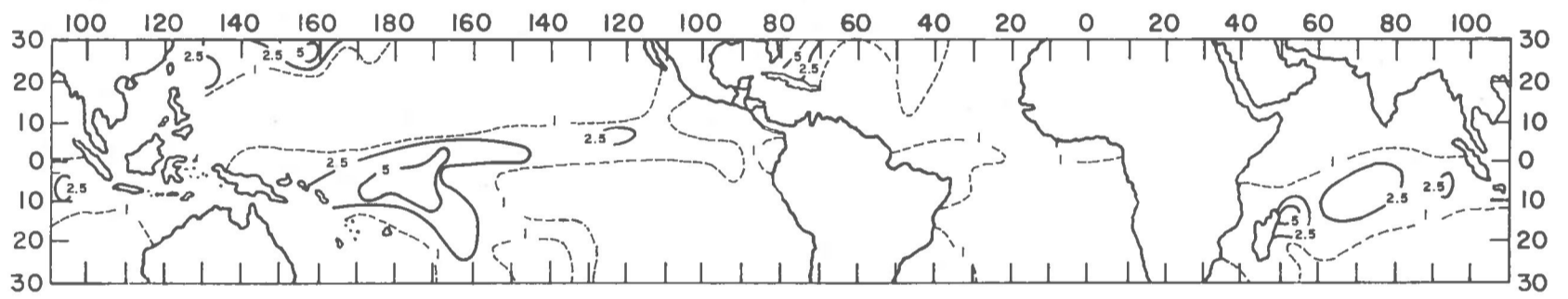
Figure 23. Frequency of heavy precipitation for the season December 1972 through February 1973. (The noon and midnight frequencies have been averaged).

contours in these three figures follow those in Figure 15, indicating
that in the tropics the fraction of rainfall occurrences in the light,
moderate, and heavy categories does not vary much from place to place;
thus precipitation amount is proportional to precipitation frequency.

4.2 Day-Night Variation

One of the most interesting problems in oceanic precipitation re-
search is the determination of its diurnal variation which, if it were
known, would provide important information about the operation of the
troposphere. Although the technique for precipitation determination
used in this study is experimental, and although the data are available
at only two local times (1130 and 2330), some insight into the diurnal
variation of oceanic precipitation frequency can be gained. Figures
24 and 25 show the frequencies of noon and midnight precipitation
(using the 0.25 mm hr^{-1} thresholds). The similarity in the two figures
indicates that there is no large difference in the frequencies of noon
and midnight precipitation. Table 5 shows the ratio of the noon precip-
itation frequency (D) to the sum of D and the midnight precipitation
frequency (N) for both dry and wet oceanic regions between $20^{\circ}N$ and
$30^{\circ}S$. The generally small difference between noon and midnight pre-
cipitation frequency is consistent with the results of Lavoie (1963) and
Jacobson and Gray (1976) who analyzed precipitation data from small
tropical islands and found an early morning maximum, a late afternoon
minimum and little difference between noon and midnight. It is inter-
esting, however, that in both wet and dry regions, higher rainfall
rates tend to occur more often near local noon than near local midnight.
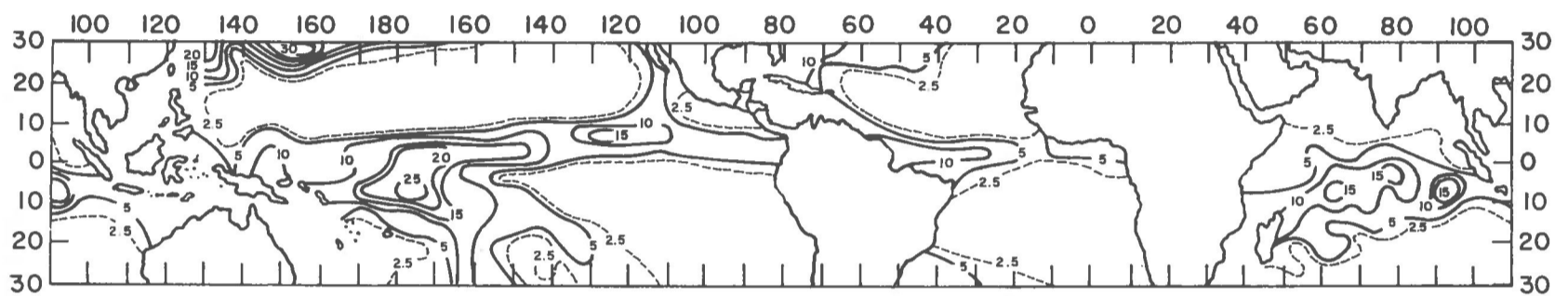
Figure 24. Frequency of precipitation near local noon for the season December 1972 through February 1973.
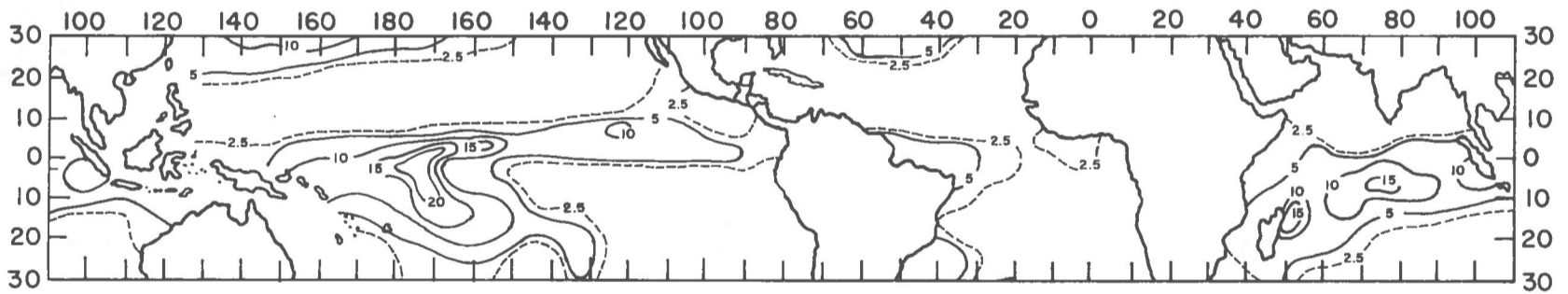
Figure 25. Frequency of precipitation near local midnight for the season December 1972 through February 1973.

TABLE 5

Fraction of the Total of Noon and Midnight
Precipitation Events Occuring near Local
Noon in Oceanic Regions Between 20°N and 30°S

$$\frac{D}{D+N} \ (\%)$$

Rainfall Category	Dry Regions (0-5%)*	Wet Regions (5-100%)*	All Regions (0-100%)*
Light Rain	47	50	48
Moderate Rain	48	52	49
Heavy Rain	49	54	51
Very Heavy Rain**	53	61	57
All rain	49	52	50

* Precipitation frequencies
** Defined by the 5.0 mm hr^{-1} threshold temperatures in Table 4

5.0 SUMMARY AND CONCLUSIONS

Tropical oceanic precipitation frequencies have been obtained from Electrically Scanning Microwave Radiometer Data with the use of theoretical threshold brightness temperatures. The generally good agreement between the results of this study and both climatological precipitation frequency and frequencies of highly reflective clouds from concurrent visible satellite data indicate that passive microwave radiometry from satellites can be a valuable tool in the determination of oceanic precipitation.

For the period 22 December 1972 through February 1973 it was found that:

1. Tropical oceanic precipitation is organized into rather narrow convergence zones near the equator. The subtropical and eastern oceans are relatively dry.

2. The difference between local noon and local midnight precipitation frequencies is small, but heavier rainfall rates tend to occur more frequently near local noon.

3. The ratios of light, moderate, and heavy precipitation frequencies seem to vary only slightly throughout tropical oceanic regions.

REFERENCES

Battan, L. J., 1973: Radar Observation of the Atmosphere. University
    of Chicago Press, Chicago, pp. 64-83.

Chandrasekhar, S., 1960: Radiative Transfer. Dover Publications, Inc.,
    New York, 393 pp.

Crutcher, H. L., and O. M. Davis, 1969: U.S. Navy Marine Climatic
    Atlas of the World, Vol. 8. NAVAIR 50-1C-54, Naval Weather Service
    Command, Washington D.C., chart 137.

Deirmendjian, D., 1963: Complete Microwave Scattering and Extinction
    Properties of Polydispersed Cloud and Rain Elements. Rand Corpora-
    tion Report 12-422-PR, Santa Monica, California, 54 pp.

Dittberner, G. J., and T. H. Vonder Haar, 1973: Large-scale precipita-
    tion estimates using satellite data; application to the Indian
    monsoon. Arch. Met. Geoph. Biokl., Ser. B, 21, 317-334.

Fletcher, N., 1963: The Physics of Rainclouds, Cambridge University
    Press, Cambridge, 390 pp.

Herzberg, G., 1950: Molecular Spectra and Molecular Structure, I. Spec-
    tra of Diatomic Molecules, Second Edition. D. Van Nostrand Co.,
    Princeton, N. J.

Holloway, J. L. Jr. and S. Manabe, 1971: Simulation of climate by a
    global general circulation model. I. Hydrological cycle and heat
    balance. Monthly Weather Review, 99, pp. 335-370.

Jackson, J. P., 1962: Classical Electrodynamics. John Wiley and Sons,
    New York, pp. 216-220.

Jacobs, W. C., 1968: The seasonal apportionment of precipitation over
    the ocean. Association of American Geographers Yearbook, V. 30,
    pp. 63-78.

Jacobson, R. W., and W. M. Gray, 1976: Diurnal Variation of Oceanic
    Deep Cumulus Convection. Colorado State University, Atmospheric
    Science Paper no. 243, Fort Collins, Colorado.

Lavoie, R. L., 1963: Some Aspects of the Meteorology of the Tropical
    Pacific Viewed from an Attol. Hawaii Institute of Geophysics Re-
    port no. 27.

Martin, D. W. and W. D. Scherer, 1973: Review of satellite rainfall
    estimation methods. Bull. Amer. Meteorol. Soc., 54, 7, 661-674.

Mc Donald, W. F., 1938: Atlas of Climatic Charts of the Oceans. U.S.
    Dept. of Agriculture, Weather Bureau, Washington, D.C.

Nordberg, W., J. Conaway, D. B. Ross and T. Wilheit, 1971: Measurements
    of microwave emission from a foam-covered, wind-driven sea. J.
    Atmos. Sci., 28, 429-435.

Oort, A. H., and E. M. Rasmusson, 1971: Atmospheric Circulation
    Statistics. NOAA Professional Paper 5, U.S. Dept. of Commerce,
    Rockville, MD, 323 pp.

Ramage, C. S., 1975: Preliminary discussion of the meteorology of the
    1972-73 El Nino. Bull. Amer. Meteor. Soc., 56, 234-242.

Sellers, W. D., 1965: Physical Climatology. Univ. of Chicago Press,
    Chicago, 272 pp.

Shifrin, K. S., Yu. I. Rabinovich and G. G. Shchukin, 1968: Microwave
    radiation field in the atmosphere. In Transfer of Microwave Rad-
    iation in the Atmosphere, Trudy no. 222, A. I. Voeikov Main
    Geophysical Obsdrvatory, Leningrad.

Staelin, D. E., 1969: Passive remote sensing at microwave wavelengths.
    Proc. IEEE, 57, 427-439.

Taylor, R. C., 1973: An Atlas of Pacific Islands Rainfall, Hawaii In-
    stitute of Geophysics Data Report no. 25, University of Hawaii,
    Honolulu, Hawaii.

Taljaard, J. J., H. van Loon, H. L. Crutcher and R. L. Jenne, 1969:
    Climate of the Upper Atmosphere, Part 1 - Southern Hemisphere,
    vol. 1, National Center for Atmospheric Research, National Weather
    Records Center, and Dept. of Defense, Washington, D.C.

The Nimbus 5 Data Catalog, 1973: Volume 1 and 2, NASA/Goddard Space
    Flight Center, Greenbelt, MD.

Tolbert, C. W., A. W. Straiton, J. H. Douglas, 1958: Electrical Engin-
    eering Laboratory Report no. 104, University of Texas, Austin, TX.

Tucker, G. B., 1961: Precipitation over the North Atlantic Ocean.
    Quart. J. Royal Meteorol. Soc., 87, pp. 147-158.

Van Vleck, J. H., 1947: Absorption of microwaves by water vapor. Phys.
    Rev., 71, 425-433.

Westwater, E. R., 1972: Microwave Emission from Clouds. NOAA Technical
    Report ERL 219-WPL 18, NOAA/Environmental Research Laboratories,
    Boulder, CO. 66 pp.

Wilheit, T. T., 1972: The Electrically Scanning Microwave Radiometer
    (ESMR) Experiment, in The Nimbus-5 User's Guide, NASA/Goddard Space
    Flight Center, Greenbelt, MD, pp. 59-105.

Wilheit, T. T., 1975: The Electrically Scanning Microwave Radiometer
    (ESMR) Experiment, in The Nimbus 6 User's Guide, NASA/Goddard Space
    Flight Center, Greenbelt, MD., pp. 87-108.

Wilheit, T. T., M.S.V. Rao, T. C. Chang, E. B. Rodgers and J. S. Theon, 1975: The Remote Sensing of Rainfall Rates over the Oceans. Presented at the Second Conference on Atmospheric Radiation of the American Meteorological Society, Arlington, VA., October 29, 1975.

APPENDIX I

EMITTANCE OF A PLANE WATER SURFACE

Jackson (1962) calculates the amplitude of a plane electomagnetic wave which has been reflected from the interface between two dielectrics. His argument is easily extended to the case where the lower dielectric has a complex dielectric constant (a lossy dielectric). Suppose that the upper and lower dielectrics have permeabilities μ and μ' and dielectric constants κ and κ', respectively. The indicies of refraction are then

$$n = \sqrt{\mu\kappa} \qquad \text{(assumed to be real)} \qquad \text{(A1)}$$

$$n' = \sqrt{\mu'\kappa'} = \gamma - j\lambda \qquad \text{(A2)}$$

A useful quantity may be defined as

$$n_s^2 = \tfrac{1}{2}\left[\gamma^2 - \lambda^2 + n^2\sin^2 i + \sqrt{(\gamma^2-\lambda^2-n^2\sin^2 i)^2 + 4\gamma^2\lambda^2}\right] \qquad \text{(A3)}$$

where i is the angle of incidence (measured from the normal to the interface).

Snell's Law becomes

$$\frac{\sin r}{\sin i} = \frac{n}{n_s} \qquad \text{(A4)}$$

where r is the angle of refraction.

If E_0 is the amplitude of the electric field in the incident wave, E_0' that for the refracted wave (at the surface of the lossy dielectric), and E_0'' that of the reflected wave, we have for horizontally polarized radiation,

$$P \equiv \frac{\mu}{\mu'}(\frac{\tan i}{\tan r} + j\frac{\gamma\lambda}{nn_s} \sec i \sec r) \qquad (A5)$$

$$\frac{E_o'}{E_o} = \frac{2}{1+P} \qquad (A6)$$

$$\frac{E_o''}{E_o} = \frac{1-P}{1+P} \qquad (A7)$$

For vertically polarized radiation,

$$q \equiv \frac{\mu}{\mu'} (\sin 2i + 2j\frac{\gamma\lambda}{nn_s} \sin r \cos i) \qquad (A8)$$

$$\frac{E_o'}{E_o} = \frac{n}{n_s} \cdot \frac{2\sin 2i}{\sin 2r + q} \qquad (A9)$$

$$\frac{E_o''}{E_o} = \frac{q - \sin 2r}{q + \sin 2r} \qquad (A10)$$

For normal incidence (i=o), both polarizations reduce to

$$\frac{E_o'}{E_o} = \frac{2n}{n'+n} \qquad (A11)$$

$$\frac{E_o''}{E_o} = \frac{n'-n}{n'+n} \qquad (A12)$$

The emittance is given by

$$\varepsilon = 1 - \left| \frac{E_o''}{E_o} \right|^2 \qquad (A13)$$

The above applies to any plane surface; one simply needs to use the appropriate permeabilities and dielectric constants. For water, Westwater (1972) gives

$$\kappa = \kappa_\infty + \frac{\kappa_0 - \kappa_\infty}{1+(\frac{j\lambda_s}{\lambda})^{1-\Omega}} \qquad \text{(A14)}$$

where

$$\kappa_\infty = 4.5$$

$$\kappa_0 = \frac{32155.45}{T} - 29.62 \qquad \text{(A15)}$$

$$\log_{10}\lambda_s = \frac{921.0935}{T} - 2.9014 \qquad \text{(A16)}$$

and $\qquad \Omega = 0.02$

T is expressed in Kelvin, and λ in centimeters. Using (A14) in (A13) and assuming that

$$\kappa_{air} = \mu_{air} = \mu_{water} = 1 \qquad \text{(A17)}$$

gives the values in Figures 4 and 5.

APPENDIX II

ESMR FLIGHT MODEL PARAMETERS
(After Wilheit, 1972)

Antenna	
Aperture Size (Linear Array Dimension)	83.3 cm (32.80 in.)
Aperture Size (Feed Array Dimension)	85.5 cm (33.66 in.)
Number of Linear Elements.	103
Number of Slots per Element	81
Amplitude Distribution (Linear Array).	-40 db sidelobe Taylor distribution
Amplitude Distribution (Feed Array)	-35 db sidelobe Taylor distribution
Broadside Half Power Beamwidth	1.4°
Number of Beam Positions	78
Antenna Beam Efficiency.	90 to 92.7%
Beam Scan Angle	±50°
Antenna Loss	1.7 db
Beam Squint Angle	-3.2° nominal
Polarization	Linear (E vector parallel to flight direction)
Cross Polarization.	-25 to -36 db
Failsafe Angle (Non-Scanning Mode)	-13.7°
VSWR	< 1.15

Radiometer	
Center Frequency	19.35 GHz
Bandwidth IF (Nominal).	50 - 150 MHz
Bandwidth RF (Nominal)	300 MHz
Local Oscillator	19.35 GHz
Mixer Noise Figure	6.5 db
$\Delta T_{rms}/47$ ms	1.5°K
Absolute Accuracy	2°K
Dynamic Range	50 - 330°K
Calibration:	
Dicke Load	~338 ±0.1°K
Ambient Load	Local ambient
Sky Horn	< 3°K